Electronic Supplementary Material (ESI) for Catalysis Science & Technology.

Electronic Supplementary Information (ESI)

Catalytic enhancement on Ti-Zr complex oxide particles for electrochemical hydrogenation of oxalic acid to produce an alcoholic compound by controlling electronic states and local oxides structures

Miho Yamauchi,[a]* Shinichi Hata,[b] Hiroto Eguchi,[c] Sho Kitano,[a] Takashi Fukushima,[a] Manabu Higashi,[a] Masaaki Sadakiyo,[a] Kenichi Kato[d]*

[a]International Institute for Carbon-Neutral Energy Research (WPI-I2CNER), Kyushu University, Motooka 744, Nishi-ku, Fukuoka 819-0395, Japan. [b]Department of Applied Chemistry, Faculty of Engineering, Sanyo-Onoda City University, Daigakudo-ri, 1-1-1, Sanyo-Onoda, Yamaguchi 756-0884, Japan. [c]Department of Chemistry, Graduate School of Science, Kyushu University, Motooka 744, Nishi-ku, Fukuoka 819-0395, Japan. [d]RIKEN SPring-8 Center, 1-1-1 Kouto, Sayo-cho, Sayo-gun, Hyogo 679-5148, Japan.

E-mail: yamauchi@i2cner.kyushu-u.ac.jp and katok@spring8.or.jp

Experimental details

1. Materials

Titanium (IV) isopropoxide and zirconium (IV) propoxide (ca. 70wt% in 1-Propanol), was purchased from Tokyo Chemical Industry Co., Ltd. ; methanol (99.5%), sulfuric acid (95.0%), oxalic acid (OX, 98.0%), glyoxylic acid monohydrate (GO, 95.0%), glycolic acid (GC, 97.0%) acetone (super dehydrated for organic synthesis) and sodium sulfate (99.0%) were purchased from Wako Pure Chemical Industries Ltd.; acetone (99.5%), sodium sulfate (99.0%) was purchased from Kanto Chemical Co., Inc.; Ti foil (99.5%) were purchased from the Nilaco Corporation. All chemicals were used without further purification. All the solutions were prepared with deionized water.

2. Preparation of $Ti_{1-x}Zr_xO_2$ complex oxide catalysts

Recently, some groups succeeded in the preparation of spherical anatase TiO_2 particles with nanometer-sized porous[1] or amorphous Ti-ZrO_2 ones[2] by solvothermal method in the limited composition range. Here, we prepared Ti-ZrO_2 complex oxide particles with a wide composition range ($Ti_{1-x}Zr_xO_2$, x=0.0, 0.005, 0.02, 0.05, 0.1, 0.15, 0.2, 0.25, 0.5, 0.75, 1.0) by a modified solvothermal method, For the preparation of $Ti_{0.9}Zr_{0.1}O_2$, titanium (IV) isopropoxide (6.0 mmol, 1.8 mL) and zirconium (IV) propoxide (0.67 mmol, 0.3 mL) were quickly added to 30 mL anhydrous acetone in a 50 mL Teflon-lined stainless-steel autoclave to avoid exposing the sample to the air, and the mixture was stirred at room temperature. The container was immediately sealed, heated from room temperature to 200 °C over 30 minutes in an electrical oven and maintained for 12 hours. The product was separated by centrifugation 6500 rpm for 5 min and washed several times with methanol and deionized water. After that, it was dried under vacuum at room temperature. Finally, as prepared catalyst was calcined at 500 ºC for 1 h under flowing air; heating rate of 100 °C /h. TiO_2 and ZrO_2, $Ti_{1-x}Zr_xO_2$ particles were also prepared in the same way.

3. Catalyst characterization

The morphology and size distribution of the catalysts were examined by observation using transmission electron microscopy (TEM, JEM-2010HCKM, JEOL) and scanning electron microscopy (SEM, JSM-IT100, JEOL). Sample grids for the TEM measurements were prepared by dropping methanol dispersions of the specimens onto a copper grid with no metal coating. The metal composition of prepared oxides was determined using an energy dispersive X-ray spectroscope (EDS, JED-2300, JEOL) equipped with the SEM instrument. Powder X-ray diffraction (XRD) patterns were obtained using synchrotron radiation (λ=1.0805 Å) at RIKEN Materials Science beamline BL44B2[3], SPring-8. Data were acquired using the high-resolution Debye–Scherrer camera equipped with an imaging plate as an X-ray detector. The nitrogen adsorption/desorption isotherms were mesdured at 77 K using a BELSORP-max (MicrotracBEL). Specific surface area and average pore size of catalysts were calculated using Bruner-Emmett-Teller (BET). The samples were pressed into pellets (3 mm diameter) at a pressure of 500 kg. The pellets were pasted gold (Au paste No.8560, TOKURIKI HONTEN CO., LTD) with gold wire (50 μm diameter Au wire, TANAKA DENSHI KOGYO K. K.), and then the pellets were dried at 60 °C under N2 atmosphere. Alternating current (AC) impedance measurement was conducted using an SI1260 impedance analyzer with 1296 dielectric interface (Solartron) in the frequency range of 1 ‐ 107 Hz under N_2 atmosphere. The measurement was conducted after the pellet was kept at a selected temperature over 30 min so that the thermal equilibrium was reached. The diffuse reflectance spectra of samples were recorded using a UV-vis spectra (V-670 spectrometer, JASCO). The diffuse reflection spectra were converted into reflectance spectra using the Kubelka-Munk function. X-ray photoelectron spectroscopy (XPS) and Ultraviolet photoelectron spectroscopy (UPS) studies were performed on a VersaProbeII (ULVAC-PHI) using non-monochromatic Al $K\alpha$ radiation and He I emission line, respectively. Binding energies in XPS spectra were corrected by referring a C 1s binding energy of the carbon atoms of the ligand in the specimens at 284.6 eV. The obtained XPS spectra were reproduced using a combination of Gaussian and Lorentzian functions. To separate the high binding energy (low kinetic energy) cut-off from the analyzer a bias voltage of -10 V was applied to the specimen in UPS measurements. An energy value of the cut off or valence band maximum (VBM) was estimated from an intersection position between a spectral baseline and a tangential line for the left or right side of a spectrum. The emission width, w, from the cut-off to VBM was used to calculate an ionization energy (*IE*) by subtracting a w value from 21.2 eV, that is photon energy of He I line.[4]

4. Electrocatalytic test

Ti foil was used as a cathode electrode substrate. Suspensions of 10 mg as prepared catalyst in methanol (0.2 mL) were applied to Ti foils (2 × 2 cm^2) previously processed at 450 ºC under air for 1 h. The catalyst mounted Ti foils were calcined at 500 ºC for 1 h under flowing air; heating rate of 100 °C /h.

Cyclic voltammograms (CV) of 0.03 M OX in a 0.2 M Na_2SO_4 solution at 50 ºC were recorded using a VersaSTAT4 potentiostat. The three-electrode system, consisting of a prepared catalyst loading electrode (working electrode area: 4 cm^2), a counter electrode of platinum wire (230×0.5 mm, BAS), and a Ag/AgCl reference electrode (RE-1B, BAS), was used for CV measurements. Ar gas was bubbled for 30 min in order to purge the air from inside of the cell. The sweeping rate was 10 mV/s. The CV measurement for a blank solution (0.2 M Na_2SO_4 solution) was carried out by following the same procedures. The pH value of the solution was adjusted by adding H_2SO_4 solution. Potentials applied to the working electrode were measured against a reference electrode and converted to the RHE reference scale using: E (versus RHE) = E (versus Ag/AgCl) + 0.199 V + 0.059 V × pH.

Chronoamperometry (CA) measurements for electrochemical reduction of OX were performed by using the three-electrode system applied for CV measurements and a two-compartment cells, where the cathode and anode were separately mounted in each cell. A piece of proton-conducting membrane (Nafion®, NRE-212, Sigma-Aldrich) was used as a separator between glass compartment cells. Ar gas was bubbled for 30 min in order to purge the air from inside of the cell. The area of the membrane was 0.95 cm^2 and the distance between working and counter electrodes was approximately 10 cm. The catalytic tests were performed at -0.7 V vs. RHE at 50 °C for 2 h. The reaction solution 50 μL was collected from the cathodic cell and analysed using a high-performance liquid chromatograph (HPLC, LC-20AD, Shimadzu) equipped with a refractive-index detector (RID-10A, Shimadzu) and a diode-array detector (SPD-M20A, Shimadzu). The gas component evolved during the reaction was determined by gas chromatograph (GC8A, Shimadzu). The Faradaic yield in the electroreduction experiments is defined by the following equation:

$$\text{Faradaic yield (\%)} = \frac{m_{\text{products}} \times n \times F}{Q} \times 100,$$

where m_{products} is the moles of reduction products; n represents the number of electrons required for the formation of glyoxylic acid (GO) and **GC** from **OX** (n=2 and 4 for the formation of GO and **GC**, respectively); F is Faraday's constant (96,485 C/mol of electrons); and Q is the total charge in Coulombs passed across the electrode during the electrolysis.

5. Atomic pair distribution function analysis

The atomic pair distribution functions (PDFs) analysis based on synchrotron X-ray total scattering (SXTS) was employed to obtain local structure information, namely, the deviation of atomic positions from average structure. SXTS data of all the samples were measured using the Debye-Scherrer camera with an imaging-plate detector installed at the RIKEN Materials Science beamline BL44B2[3] of SPring-8. Incident X-rays of 0.69 Å were used to suppress the generation of fluorescent X-rays from the element Zr, which has the K absorption edge around 0.689 Å. To obtain high-resolution PDFs, SXTS data were acquired in a wide range of 2θ up to 150°, which corresponds to about 18 Å^{-1} in Q (=4πsinθ/λ), by rotating the imaging-plate stage by 70° from its initial position. The measurement time was 20 min for each sample and each position. In addition to the glass capillaries filled with the powder samples, an empty capillary with the same size and materials was measured under same conditions to discriminate between background and diffuse scattering for the PDF analysis. The PDFs for all the samples were obtained on the basis of Fourier transform of normalized and corrected SXTS data with xPDFsuite[5].

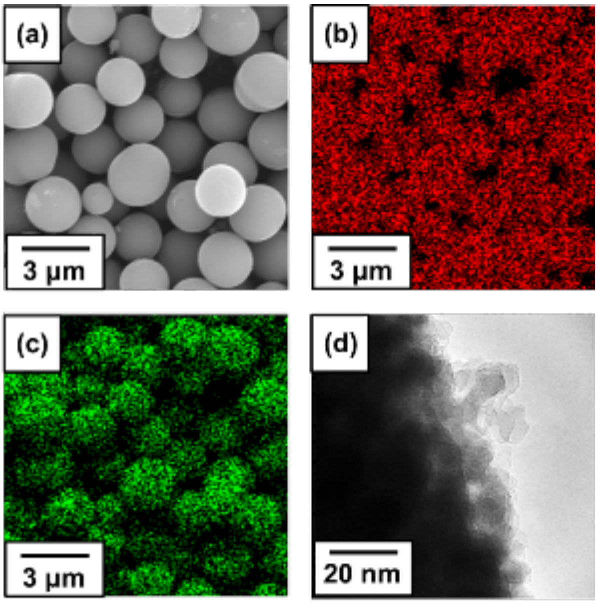

Figure S1. SEM (a: low-magnification), SEM-EDS (b: Ti-K signal, c: O-K signal) and TEM (d: high-magnification) images of TiO_2 particles (x=0.0).

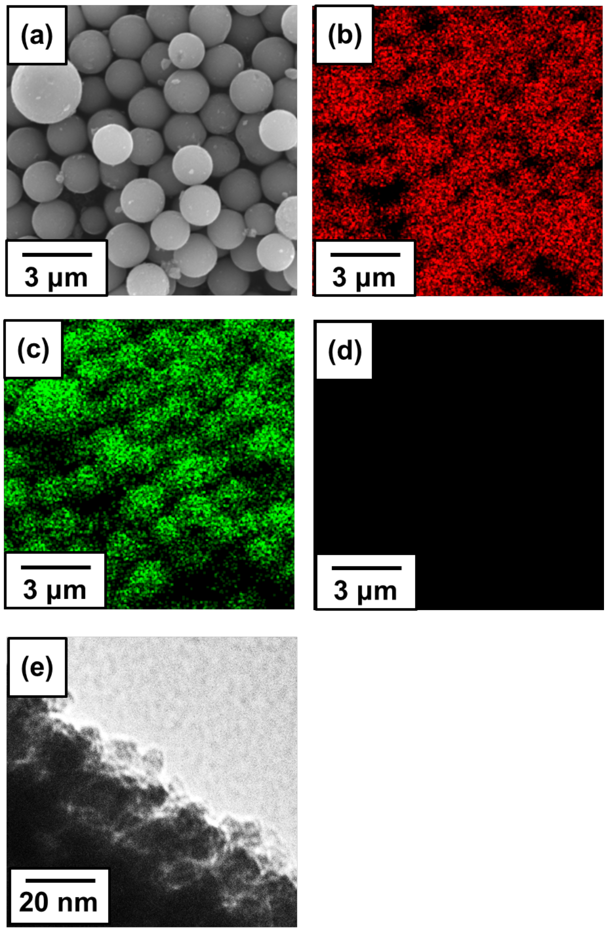

Figure S2. SEM (a: low-magnification), SEM-EDS (b: Ti-K signal, c: O-K signal, d: Zr-K signal,) and TEM (e: high-magnification) images of $Ti_{0.995}Zr_{0.005}O_2$ particles (x=0.005).

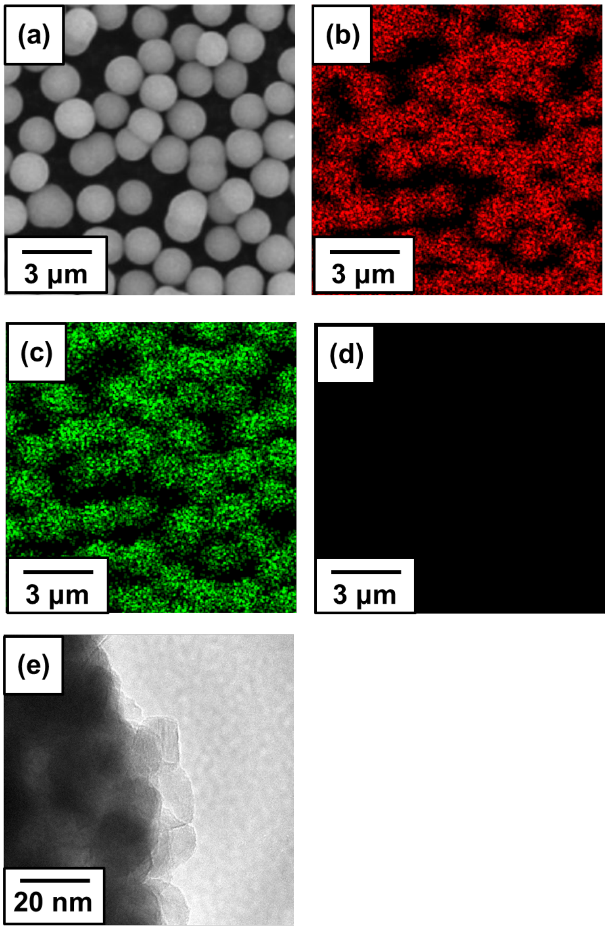

Figure S3. SEM (a: low-magnification), SEM-EDS (b: Ti-K signal, c: O-K signal, d: Zr-K signal,) and TEM (e: high-magnification) images of $Ti_{0.98}Zr_{0.02}O_2$ particles (x=0.02).

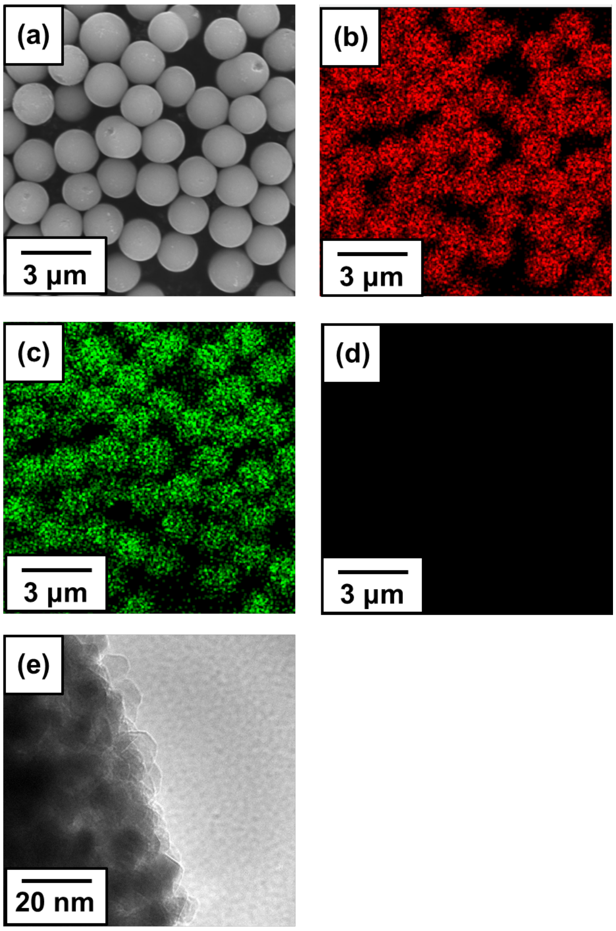

Figure S4. SEM (a: low-magnification), SEM-EDS (b: Ti-K signal, c: O-K signal, d: Zr-K signal,) and TEM (e: high-magnification) images of $Ti_{0.95}Zr_{0.05}O_2$ particles (x=0.05).

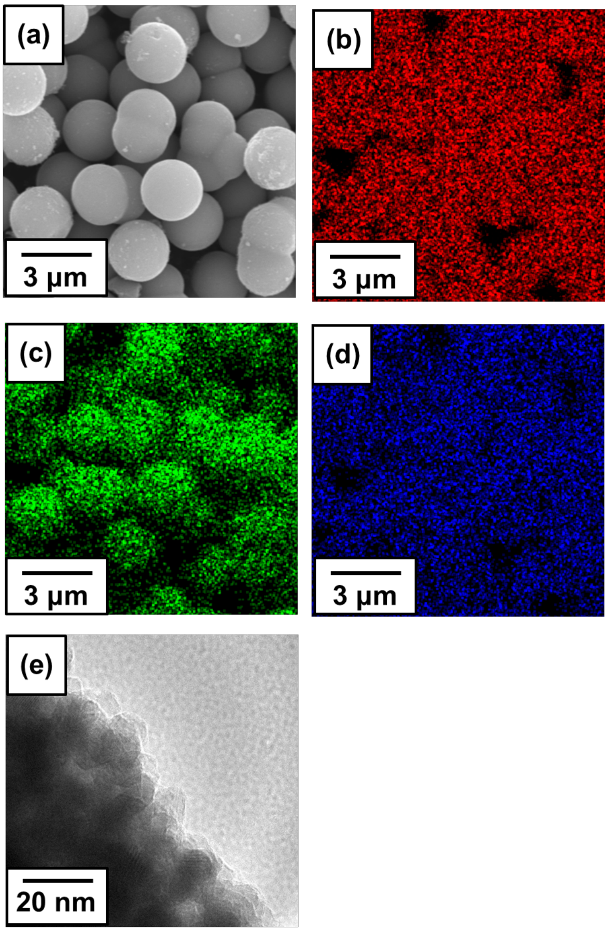

Figure S5. SEM (a: low-magnification), SEM-EDS (b: Ti-K signal, c: O-K signal, d: Zr-K signal,) and TEM (e: high-magnification) images of $Ti_{0.9}Zr_{0.1}O_2$ particles (x=0.1).

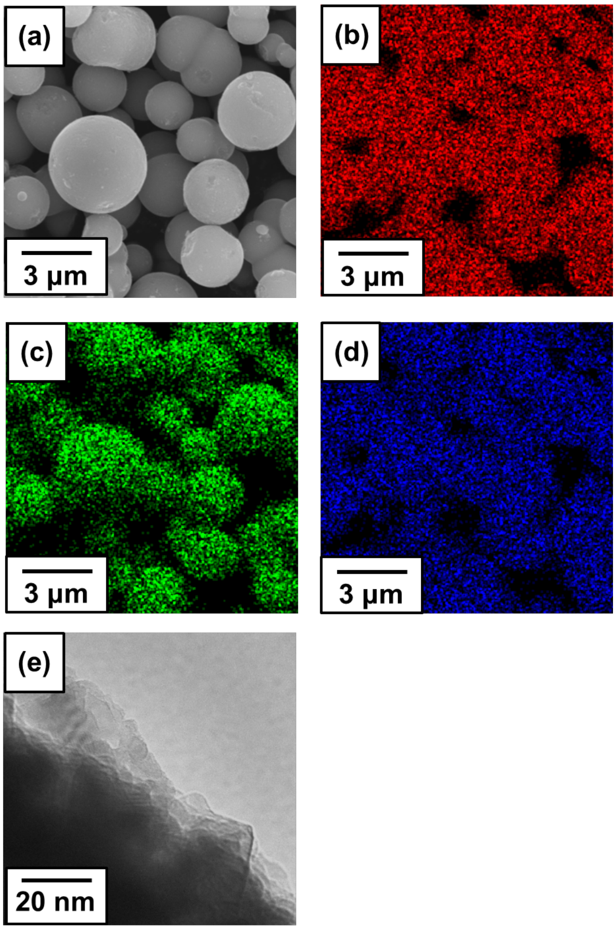

Figure S6. SEM (a: low-magnification), SEM-EDS (b: Ti-K signal, c: O-K signal, d: Zr-K signal,) and TEM (e: high-magnification) images of $Ti_{0.85}Zr_{0.15}O_2$ particles (x=0.15).

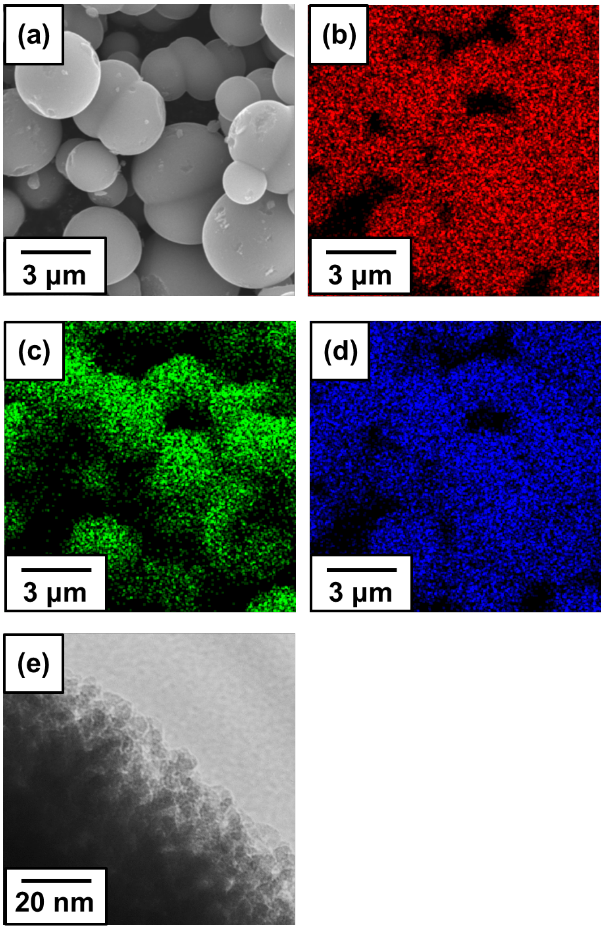

Figure S7. SEM (a: low-magnification), SEM-EDS (b: Ti-K signal, c: O-K signal, d: Zr-K signal,) and TEM (e: high-magnification) images of $Ti_{0.8}Zr_{0.2}O_2$ particles (x=0.2).

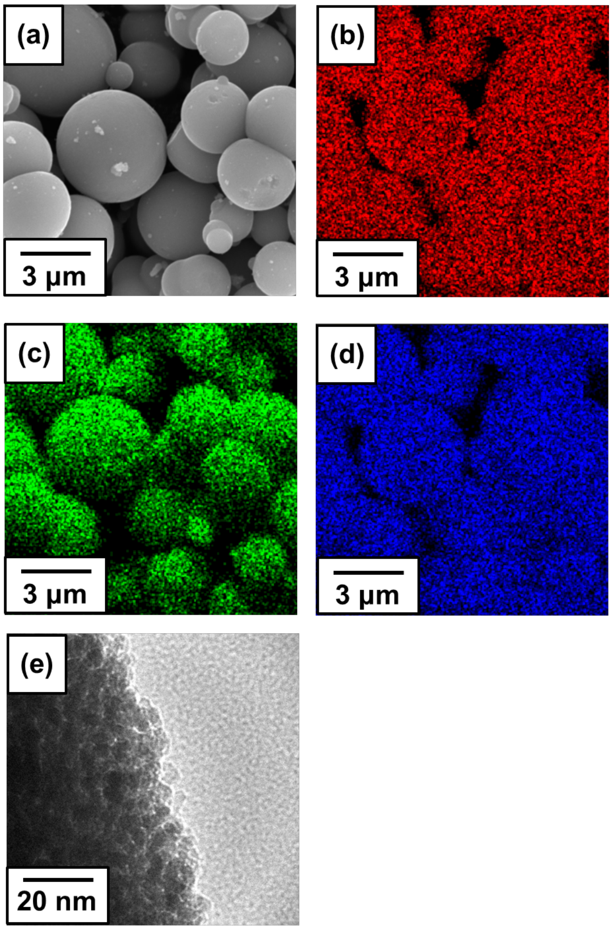

Figure S8. SEM (a: low-magnification), SEM-EDS (b: Ti-K signal, c: O-K signal, d: Zr-K signal,) and TEM (e: high-magnification) images of $Ti_{0.75}Zr_{0.25}O_2$ particles (x=0.25).

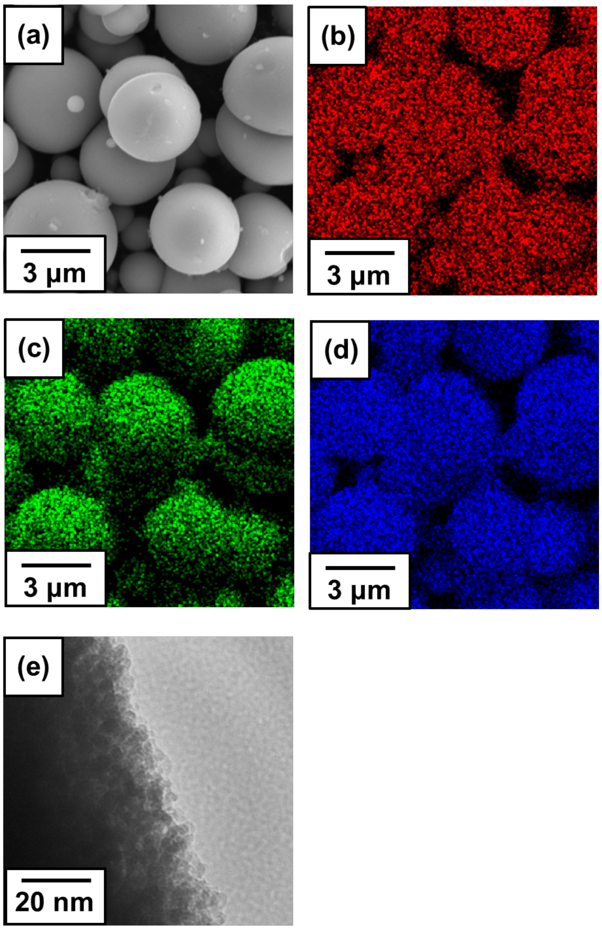

Figure S9. SEM (a: low-magnification), SEM-EDS (b: Ti-K signal, c: O-K signal, d: Zr-K signal,) and TEM (e: high-magnification) images of $Ti_{0.5}Zr_{0.5}O_2$ particles (x=0.5).

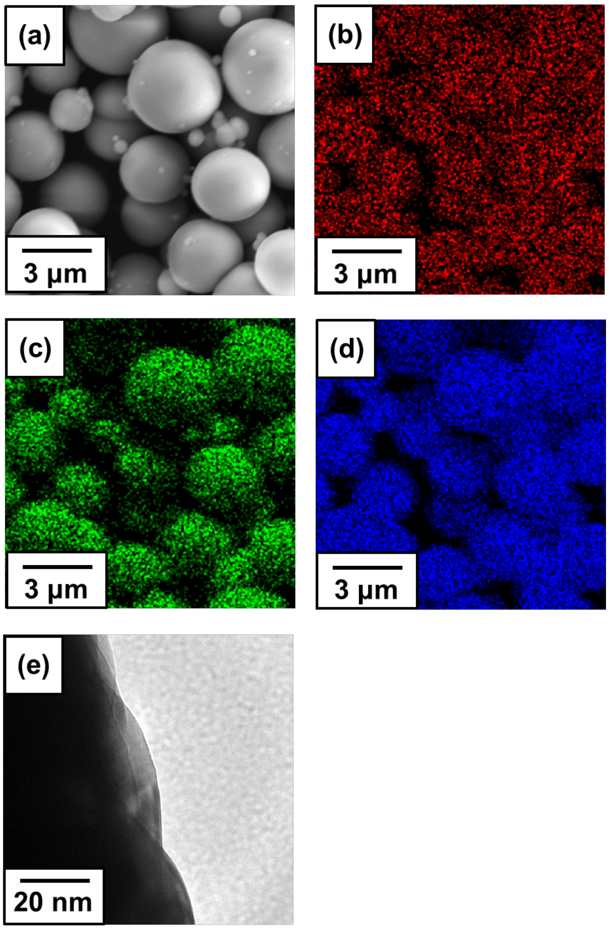

Figure S10. SEM (a: low-magnification), SEM-EDS (b: Ti-K signal, c: O-K signal, d: Zr-K signal,) and TEM (e: high-magnification) images of $Ti_{0.25}Zr_{0.75}O_2$ particles (x=0.75).

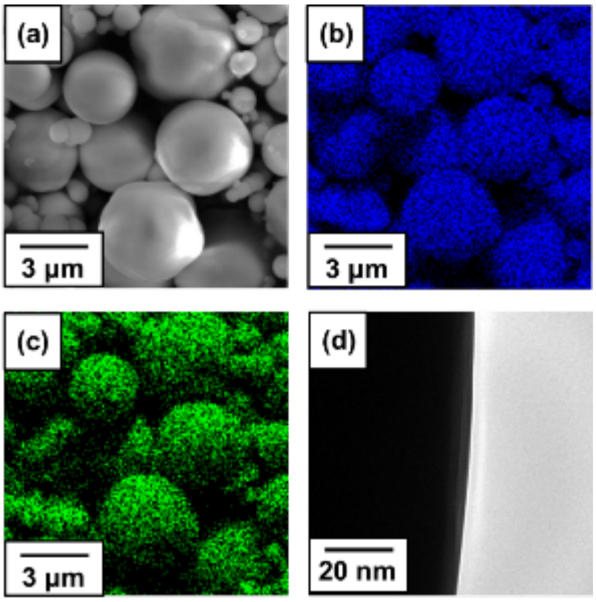

Figure S11. SEM (a: low-magnification), SEM-EDS (b: Zr-K signal, c: O-K signal) and TEM (d: high-magnification) images of ZrO_2 particles (x=1.0).

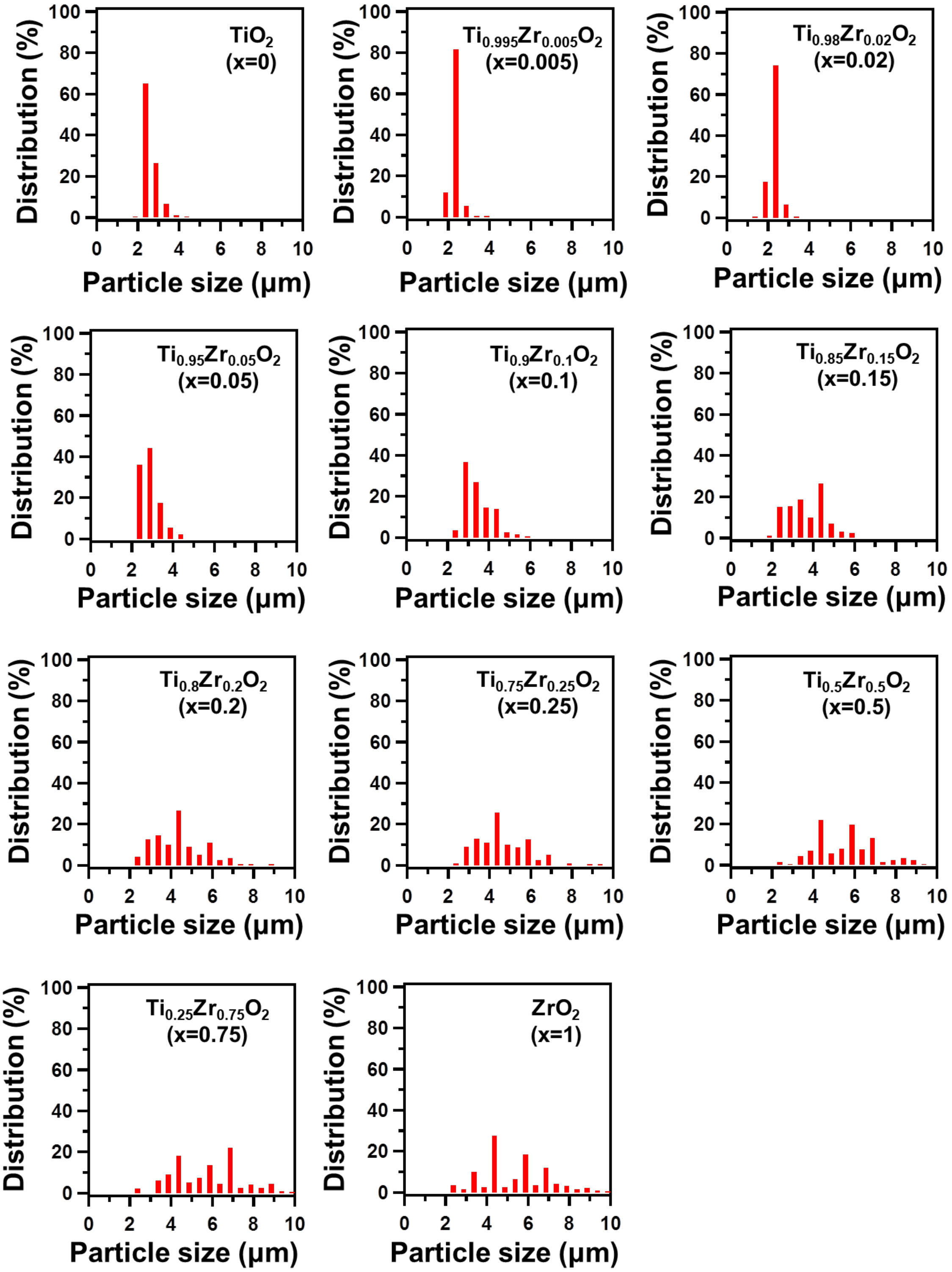

Figure S12. Size distributions of Ti-ZrO$_2$ particles.

Table S1. Composition of Ti-ZrO_2 particles.

Ti-ZrO_2 samples	TiO_2:ZrO_2 molar percent by EDS results
TiO_2	100:0
$Ti_{0.995}Zr_{0.005}O_2$	99.3:0.69
$Ti_{0.98}Zr_{0.02}O_2$	97.7:2.3
$Ti_{0.95}Zr_{0.05}O_2$	94.6:5.4
$Ti_{0.9}Zr_{0.1}O_2$	90.3:9.7
$Ti_{0.85}Zr_{0.15}O_2$	84.0:16.0
$Ti_{0.80}Zr_{0.20}O_2$	79.4:20.6
$Ti_{0.75}Zr_{0.25}O_2$	76.0:24.0
$Ti_{0.5}Zr_{0.5}O_2$	50.2:49.8
$Ti_{0.25}Zr_{0.75}O_2$	25.1:74.9
ZrO_2	0:100

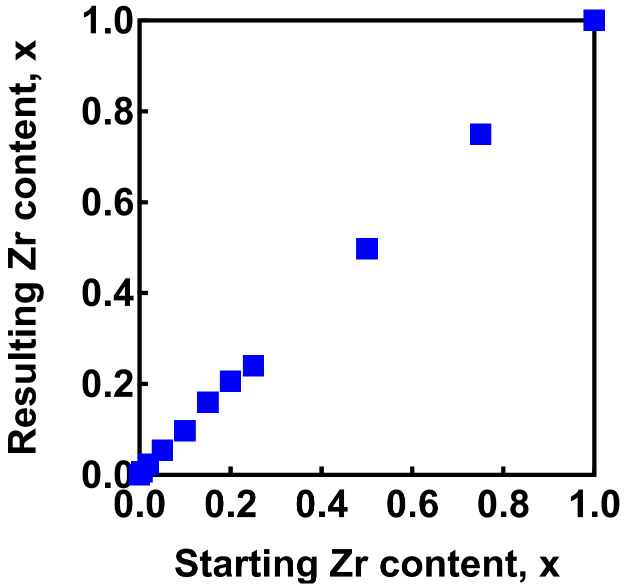

Figure S13. Resulting Zr content (x) in $Ti_{1-x}Zr_xO_2$ particles.

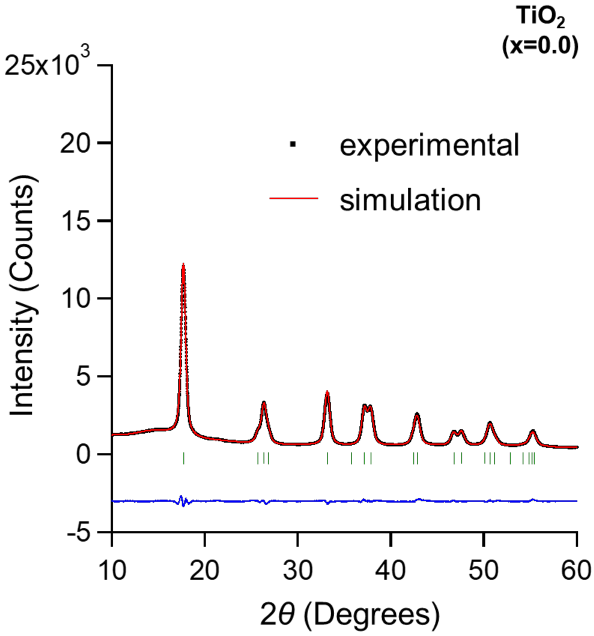

Figure S14. XRD pattern for TiO$_2$ particle (black), Rietveld profile curve (red), calculated peak positions (green for anatase phase), the difference between experimental and simulated curve (blue).

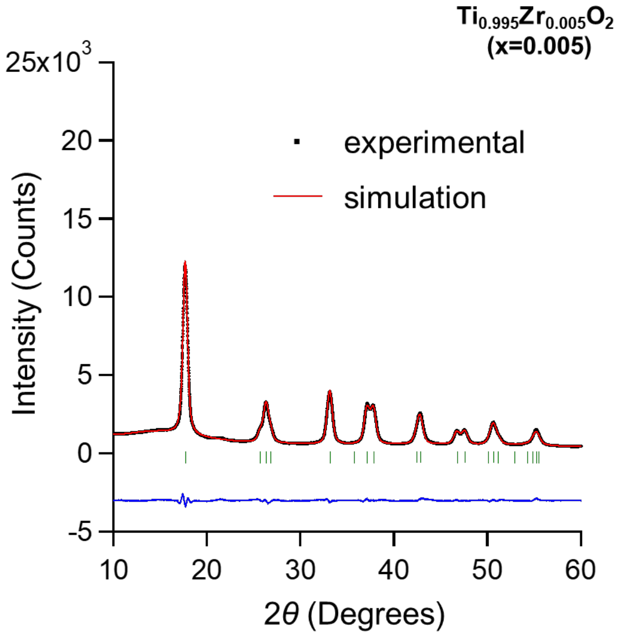

Figure S15. XRD pattern for Ti$_{0.995}$Zr$_{0.005}$O$_2$ particles (black), Rietveld profile curve (red), calculated peak positions (green for anatase phase), the difference between experimental and simulated curve (blue).

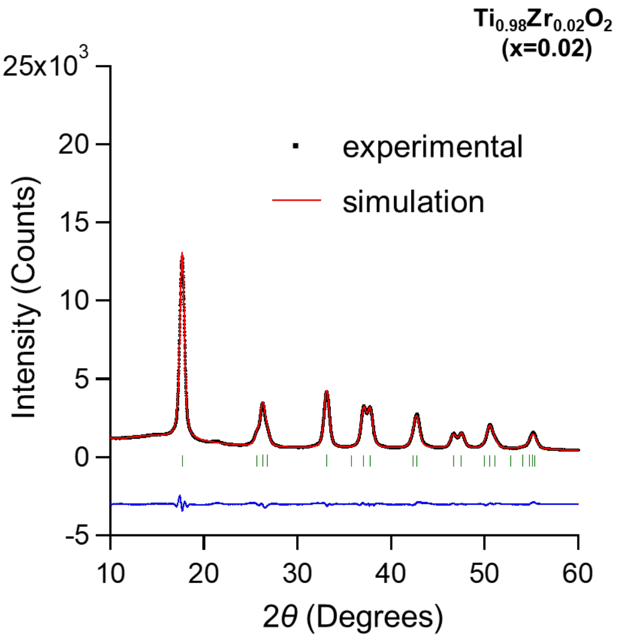

Figure S16. XRD pattern for $Ti_{0.98}Zr_{0.02}O_2$ particles (black), Rietveld profile curve (red), calculated peak positions (green for anatase phase), the difference between experimental and simulated curve (blue).

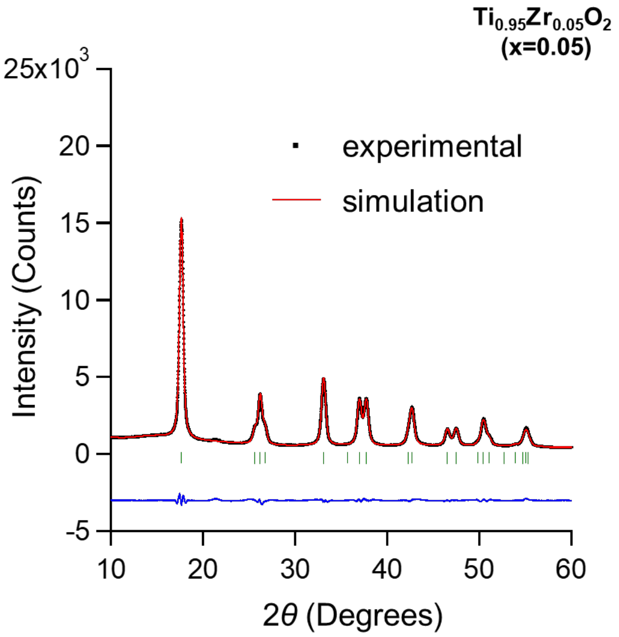

Figure S17. XRD pattern for $Ti_{0.95}Zr_{0.05}O_2$ particles (black), Rietveld profile curve (red), calculated peak positions (green for anatase phase), the difference between experimental and simulated curve (blue).

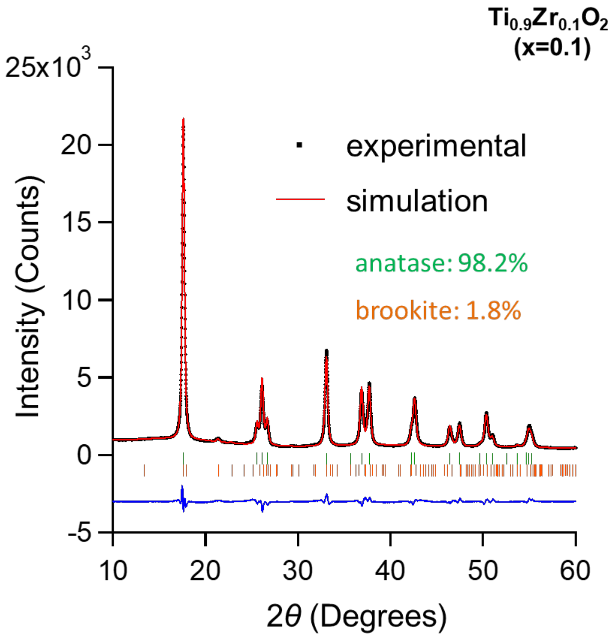

Figure S18. XRD pattern for $Ti_{0.9}Zr_{0.1}O_2$ particles (black), Rietveld profile curve (red), calculated peak positions (green for anatase phase and orange for brookite one), the difference between experimental and simulated curve (blue).

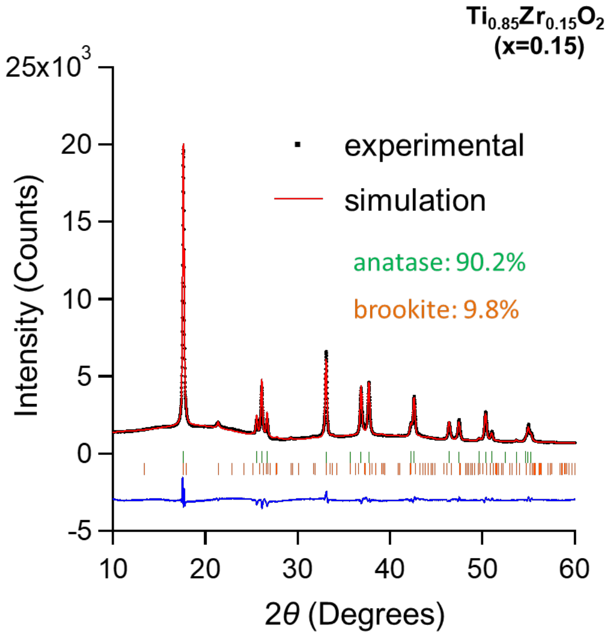

Figure S19. XRD pattern for $Ti_{0.85}Zr_{0.15}O_2$ particles (black), Rietveld profile curve (red), calculated peak positions (green for anatase phase and orange for brookite one), the difference between experimental and simulated curve (blue).

Table S2. Structural parameters of $Ti_{1-x}Zr_xO_2$ particles.

x	0	0.005	0.02	0.05	0.1		0.15	
percentage (%)	100	100	100	100	98.17	1.83	90.21	9.79
crystal system	Tetragonal	Tetragonal	Tetragonal	Tetragonal	Tetragonal	Orthorhombic	Tetragonal	Orthorhombic
space group	I41/amd	I41/amd	I41/amd	I41/amd	I41/amd	Pbca	I41/amd	Pbca
a (Å)	3.7878(7)	3.7908(0)	3.7931(3)	3.7954(5)	3.8000(1)	9.1531(4)	3.7987(6)	9.2456(2)
a (Å)	-	-	-	-	-	5.4808(1)	-	5.4597(8)
c (Å)	9.4899(3)	9.4990(7)	9.5517(2)	9.5370(4)	9.5716(1)	5.2332(1)	9.5760(6)	5.1620(2)
V (Å^3)	136.16(1)	136.50(3)	136.85(3)	137.38(5)	138.21(5)	262.53(2)	138.18(7)	260.56(9)
T (K)	298	298	298	298	298		298	
R_p	2.00	2.38	2.49	2.34	3.64		3.47	
R_{wp}	2.56	3.00	3.24	3.09	4.76		4.50	
2θrange	10.0-60.0	10.0-60.0	10.0-60.0	10.0-60.0	10.0-60.0		10.0-60.0	
wavelength a (Å)	1.0805	1.0805	1.0805	1.0805	1.0805		1.0805	

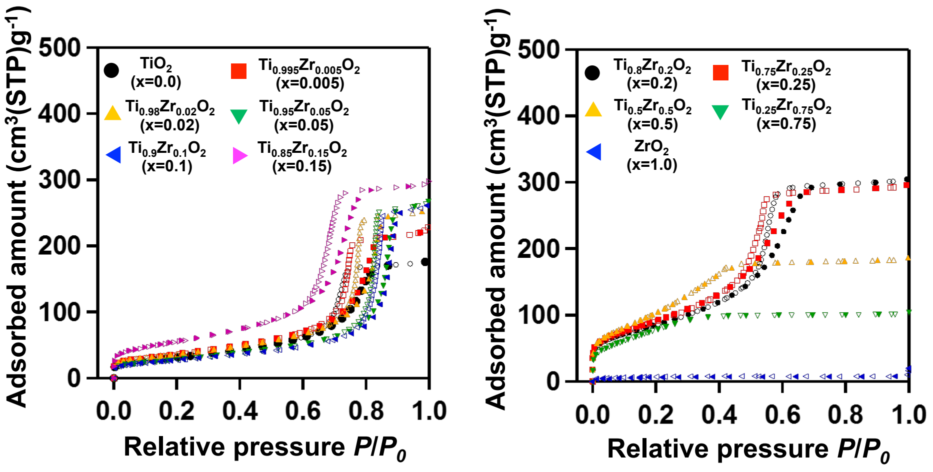

Figure S20. N_2 adsorption-desorption isotherms measured at 77 K for $Ti_{1-x}Zr_xO_2$ particles with (a)$x \leq 0.15$ and (b)$x \geq 0.2$. Closed and open symbols represent adsorption and desorption, respectively.

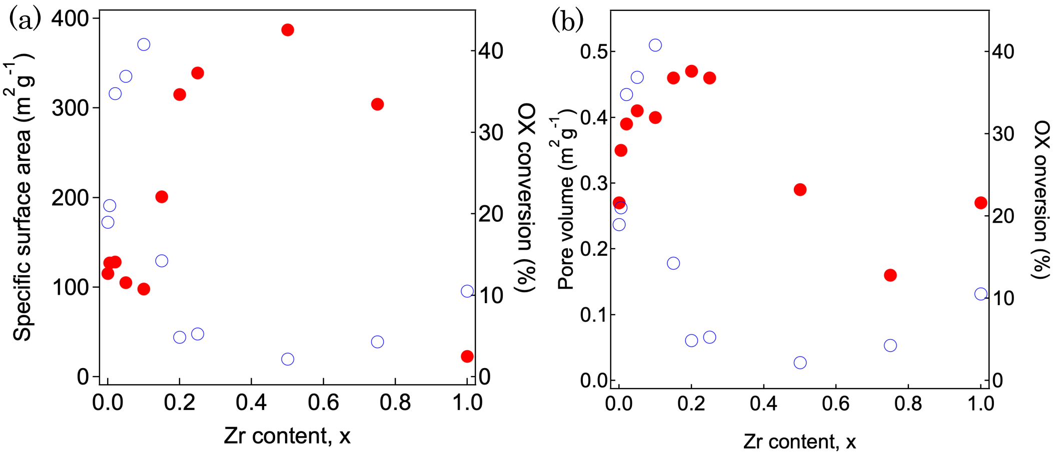

Figure S21. (a) Specific surface area (red solid circle) and (b) pore volume (red solid circle) for $Ti_{1-x}Zr_xO_2$ particles together with their OX conversion (blue open circle).

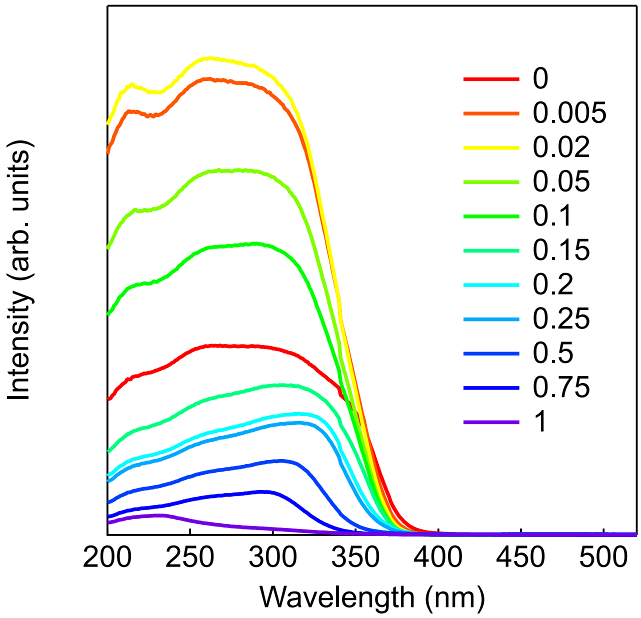

Figure S22. UV-vis diffuse reflectance spectra for $Ti_xZr_{1-x}O_2$ particles.

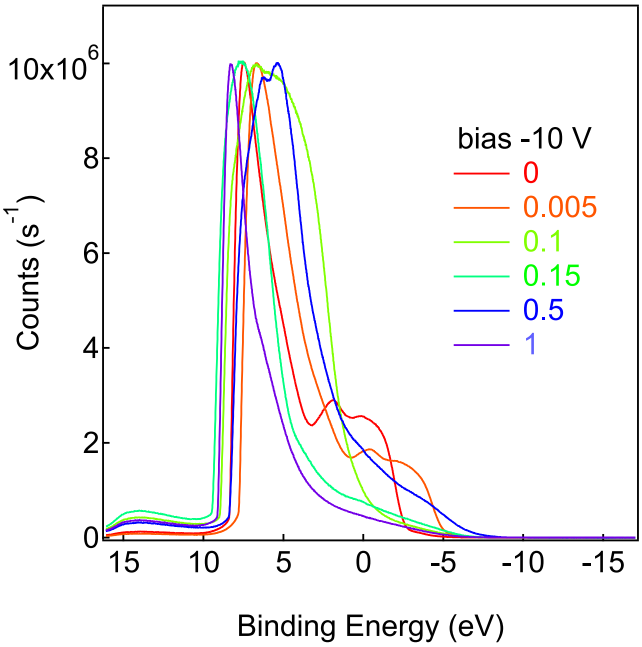

Figure S23. UPS spectra measured for $Ti_{1-x}Zr_xO_2$ with x=0, 0.005, 0.1, 0.15, 0.5 and 1.

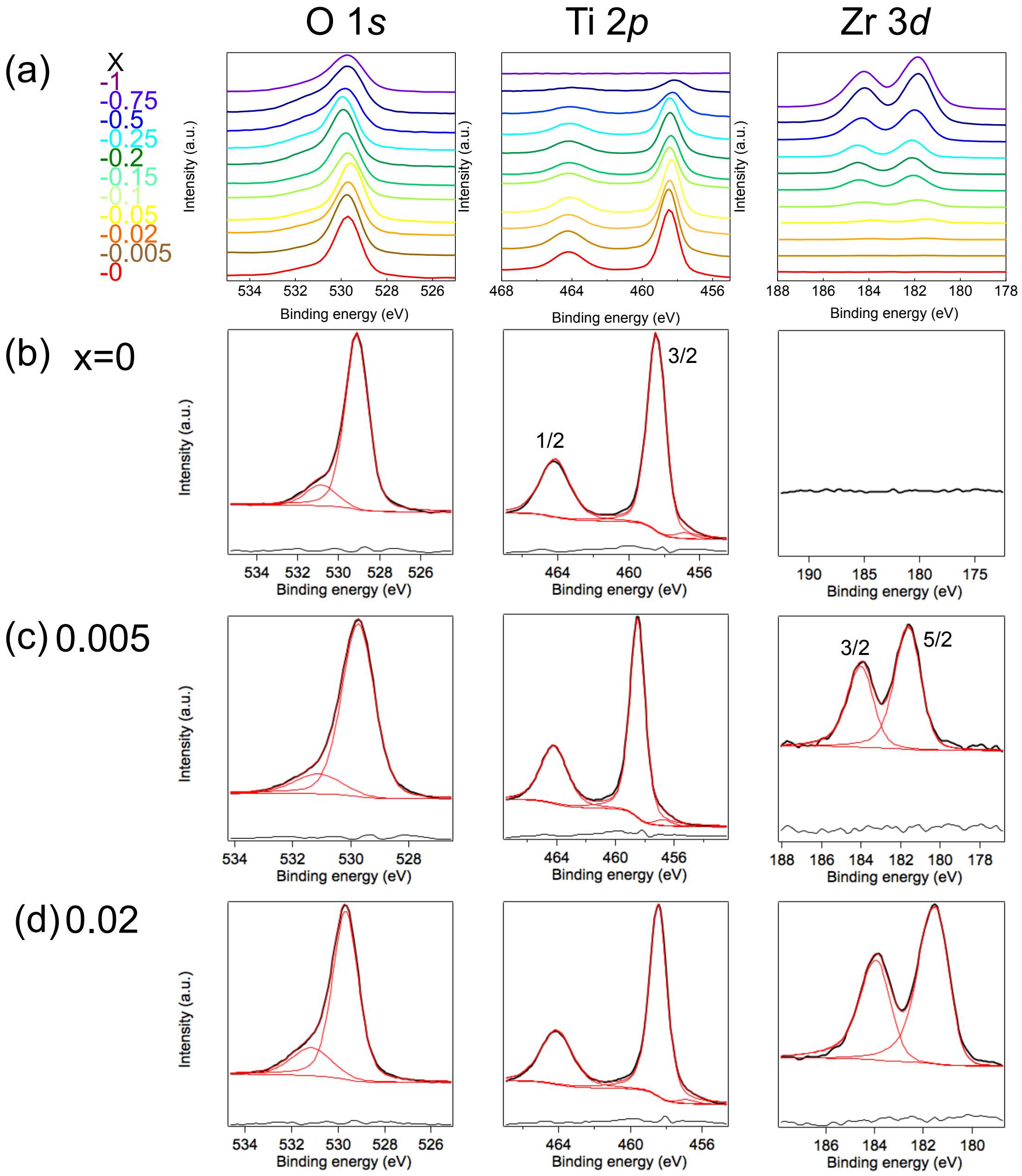
O 1s
Ti 2p
Zr 3d
(a)
x
-1
-0.75
-0.5
-0.25
-0.2
-0.15
-0.1
-0.05
-0.02
-0.005
-0
Intensity (a.u.)
Binding energy (eV)
534 532 530 528 526
468 464 460 456
188 186 184 182 180 178
(b) x=0
1/2
3/2
534 532 530 528 526
464 460 456
190 185 180 175
(c) 0.005
3/2
5/2
534 532 530 528
464 460 456
188 186 184 182 180 178
(d) 0.02
534 532 530 528 526
464 460 456
186 184 182 180

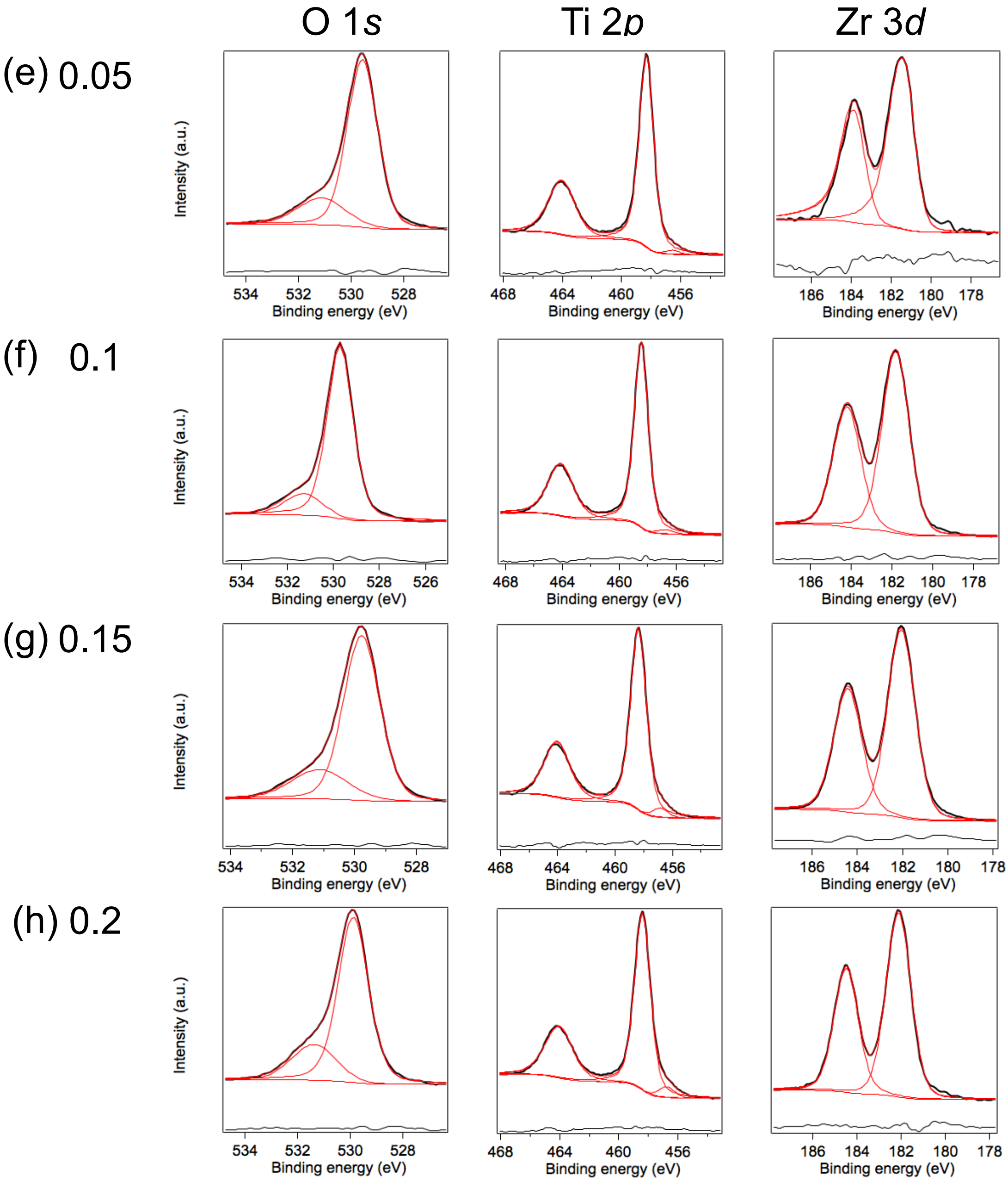
O 1*s*
Ti 2*p*
Zr 3*d*
(e) 0.05
(f) 0.1
(g) 0.15
(h) 0.2
Intensity (a.u.)
534 532 530 528
534 532 530 528 526
468 464 460 456
186 184 182 180 178
Binding energy (eV)

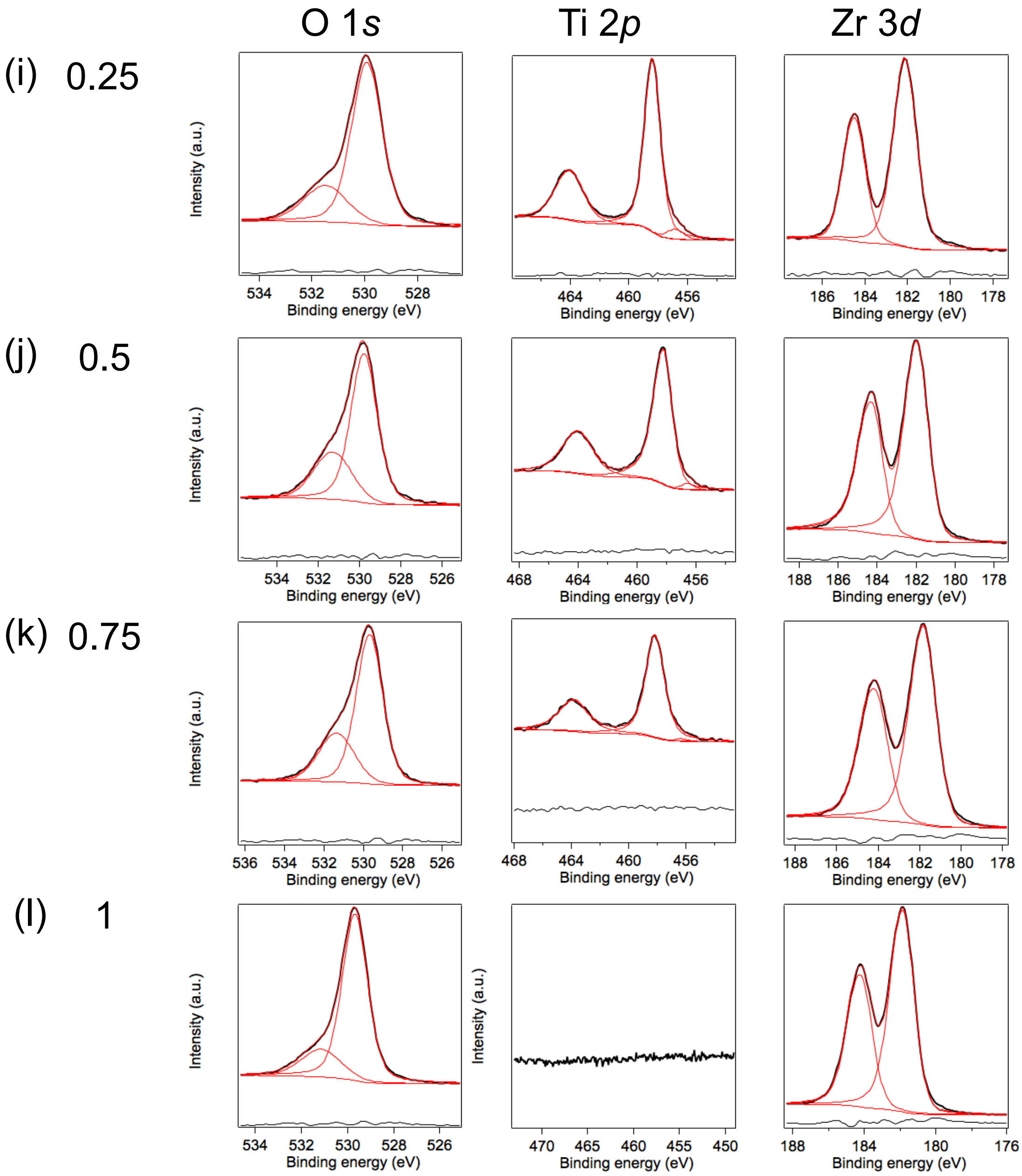

Figure S24. O1*s* (left), Ti 2*p* (center) and Zr 3*d* (right) XPS spectra for (a) all $Ti_{1-x}Zr_xO_2$ particles and observed (black) and calculated (red) spectra for $Ti_{1-x}Zr_xO_2$ particles with (b) x=0.0, (c) 0.005, (d) 0.02 (e) 0.05, (f) 0.1, (g) 0.15, (h) 0.2, (i) 0.25, (j) 0.5 (k) 0.75 and (l) 1.0. A difference between observed and calculated ones is shown at the bottom.

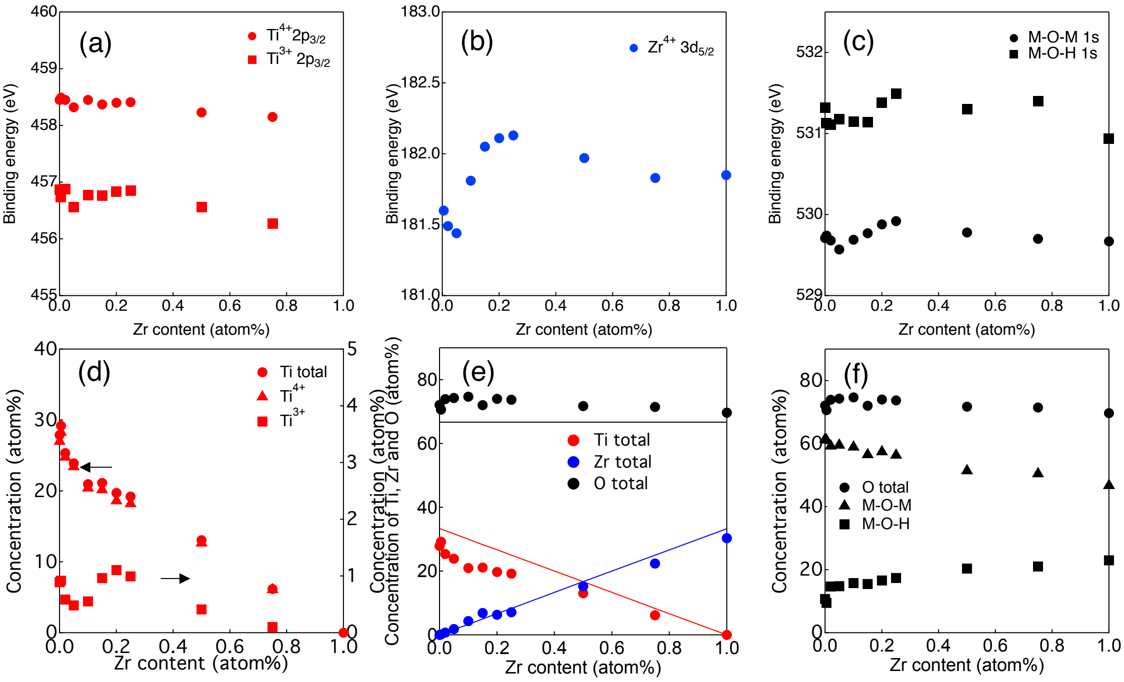

Figure S25. Binding energies of (a) Ti, (b) Zr and (c) O ions determined from XPS spectra for $Ti_{1-x}Zr_xO_2$ particles. Concentrations of (d) Ti, (e) Ti, Zr, O and (f) O species on the surface, which were determined from XPS spectra. In (e), solid lines indicate starting concentrations of Ti (red), Zr (blue) and O (black) species.

For all samples, two kinds of peaks for Ti and O species were observed. XPS signals observed around 458.5 eV and 456.7 eV can be attributed to Ti^{4+} in a lattice and Ti^{3+} at surface defects, and around 531.2 eV and 529.7 eV were attributed to an oxygen in a lattice and an oxygen of a surface hydroxyl group, respectively[6,7]. Signals observed around 181.8 eV for $Ti_xZr_{1-x}O_2$ particles with $x \geq 0.005$ can be assigned to a Zr^{4+} specie.[8,9] Although binding energies for Ti, Zr and O species changed as a function of the composition range shown in Figures S27a-c, we could not confirmed apparent relationship between catalytic performances and changes in the binding energies. Surface concentrations of Ti, Zr, and O ions were shown in Figures S27d-f. Concentration of ions on the surface agreed well with the starting composition although we could not find apparent relationship between the composition dependence and catalytic performances. Surface concentrations of Ti species were shown in Figure S27d. The percentage of Ti^{4+} species was monotonically decreased with Zr content. The percentage of Ti^{3+} ions reached the minimum around $x=0.1$ and monotonically decreased at $x \geq 0.2$, i.e., in the amorphous region. The Ti^{3+} concentration reflects formation of oxygen defects on the surface of anatase TiO_2[10]. Thus, decrease of the Ti^{3+} concentration from $x=0$ to $x=0.1$, i.e., implies decrease of surface defects and improvement of crystallinity, which is consistent with the result from XRD measurements as described above. Therefore, we can conclude that inclusion of Zr ions contributes to enhancement of crystallinitiy of whole anantaze Ti-ZrO_2 particles although relevance of valence states to catalytic performances is not confirmed. These observations clearly suggest that structural factors are more responsible than valence states for achieving notable catalytic activities.

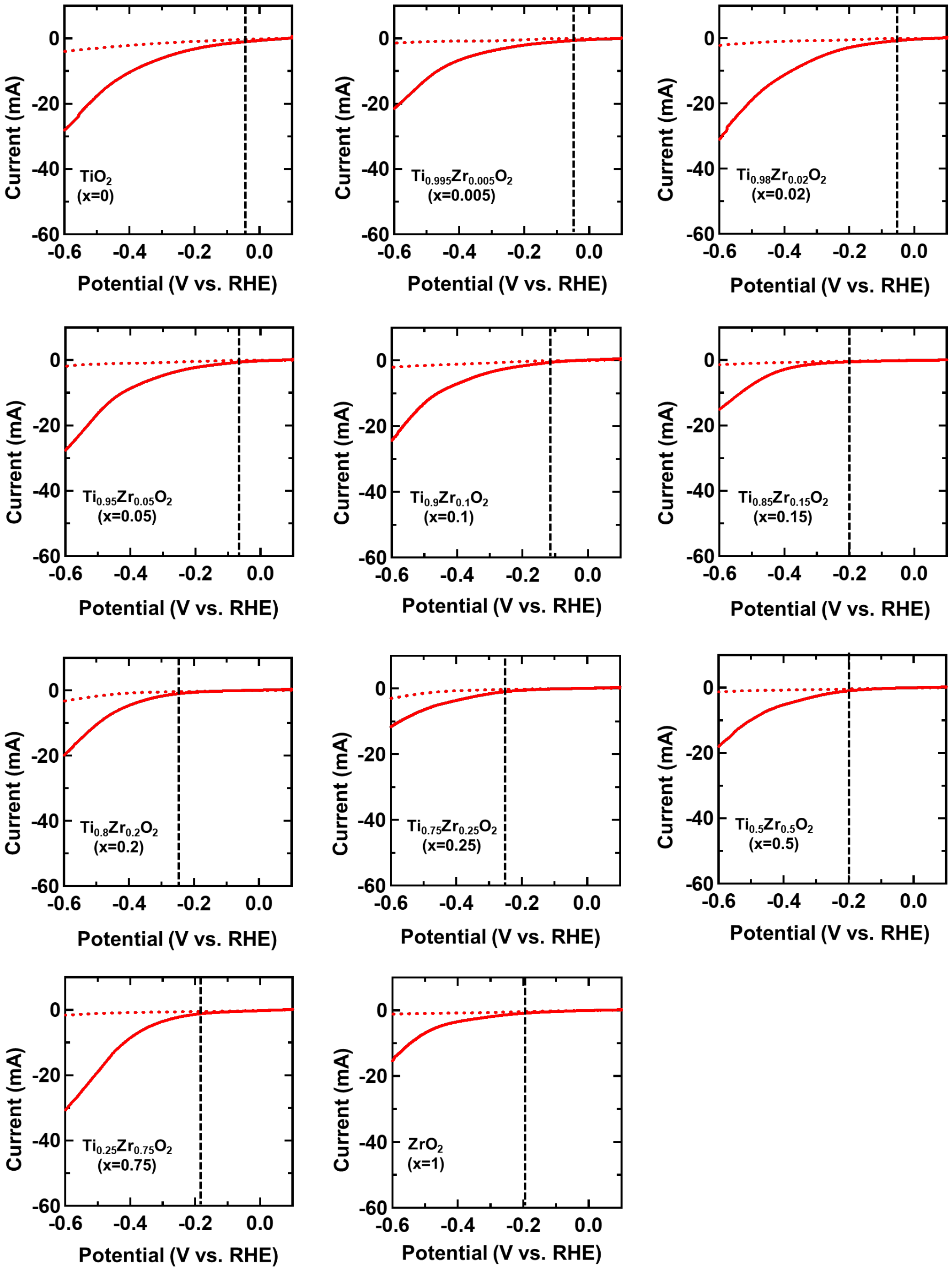

Figure S26. CV curves for the electroreduction of OX using $Ti_{1-x}Zr_xO_2$ particles. Solid and broken red curves represent reduction current measured in electrolyte solutions with and without the OX substrate, respectively. The electrochemical experiments were conducted in 0.03 M OX aqueous solution including 0.2 M Na_2SO_4 or 0.2 M Na_2SO_4 (pH 2.1) aqueous solution at 50 °C. Broken black lines indicate the onset potential for OX reduction.

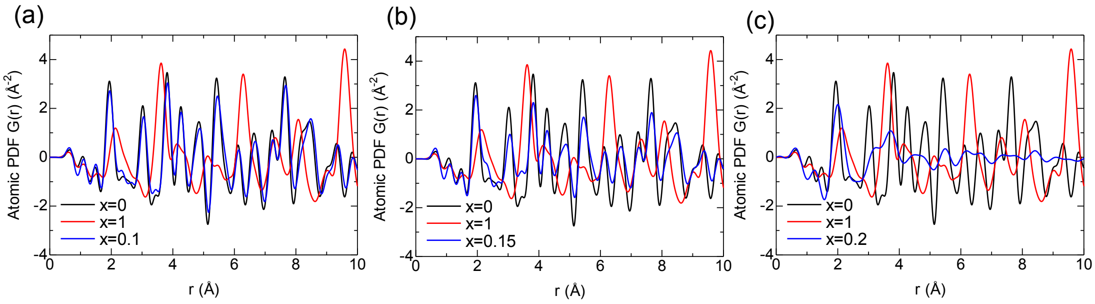

Figure S27. PDFs of (a) *x*=0.1, (b) x=0.15, and (c) x=0.2, as compared with those of x=0 and 1.

Table S3. Reaction rates and experimental conditions in hydrogenation of carboxylic acid in this study and previous reports.

Entry	Catalyst	Amount	Solvent	Substrate	Temp. (°C)	Time (h)	H_2 (MPa)	Reaction rate (μmol h^{-1})	Ref. No
1	$Ti_{0.9}Zr_{0.1}O_2$	10 mg	Na_2SO_4 aq	oxalic acid	50	2	–	319	This work
2	porous TiO_2	10 mg	Na_2SO_4 aq	oxalic acid	50	2	–	230	6
3	Re/TiO_2	0.72 g	–	various monocarboxylic acid	140-180	24	5	36-40	7
4	Re–Pd/SiO_2	150 mg	1,4-dioxane	stearic acid	140	1–3	8	30-742	8
5	Cu-Fe oxide/SiO_2	10 mg	Hexane	stearic acid	180	3	3	0.1-0.3	9
6	Pt-Re/TiO_2	0.3 g	Dodecane	long-chain fatty acids	130	1–20	2	18-2900	10
7	Iridium Complexe	2.2 mg	H_2O/HBF_4	various monocarboxylic acid	120	65	3	99-100	11
8	Ru carboxylates	1.5 mol%	Toluene	various monocarboxylic acid	160	24–48	8	14-42	12
9	Ru(acac)$_3$ and triphos	4 mol%	Toluene/H_2O	various monocarboxylic acid	160	48	6	8.5-20	13
10	$Co(BF_4)_2{\cdot}6H_2O$ and triphos	1 mol%	THF	various carboxylic acid	100	22	8	72-135	14

5. References

(1) Liu, B.; Liu, L.-M.; Lang, X.-F.; Wang, H.-Y.; Lou, X. W. D.; Aydil, E. S. *Energy Environ. Sci.* **2014**, *7*, 2592-2597.

(2) Uchiyama, H.; Matsumoto, K.; Kozuka, H. *J. Cryst. Growth* **2012**, *338*, 201-207.

(3) Kato, K.; Tanaka, H. *Adv. Phys. X* **2016**, *1*, 55-80.

(4) Diederich, L.; Küttel, O. M.; Aebi, P.; Schlapbach, L. *Surf. Sci.* **1998**, *418*, 219-239.

(5) Yang, X.; Juhas, P.; Farrow, C. L.; Billinge, S. J. *arXiv* **2015**, *1402*, 3163.

(6) Jensen, H.; Soloviev, A.; Li, Z.; Søgaard, E. G. *Appl. Surf. Sci.* **2005**, *246*, 239-249.

(7) Kumar, P. M.; Badrinarayanan, S.; Sastry, M. *Thin Solid Films* **2000**, *358*, 122-130.

(8) Mahmood, Q.; Afzal, A.; Siddiqi, H. M.; Habib, A. *J. Sol-Gel Sci. Technol.* **2013**, *67*, 670-674.

(9) Tsunekawa, S.; Asami, K.; Ito, S.; Yashima, M.; Sugimoto, T. *Appl. Surf. Sci.* **2005**, *252*, 1651-1656.

(10) Ikeda, S.; Sugiyama, N.; Murakami, S.-y.; Kominami, H.; Kera, Y.; Noguchi, H.; Uosaki, K.; Torimoto, T.; Ohtani, B. *Phys. Chem. Chem. Phys.* **2003**, *5*, 778-783.

(11) Watanabe, R.; Yamauchi, M.; Sadakiyo, M.; Abe, R.; Takeguchi, T. *Energy Environ. Sci.* **2015**, *8*, 1456-1462.

(12) Toyao, T.; Siddiki, S.; Touchy, A. S.; Onodera, W.; Kon, K.; Morita, Y.; Kamachi, T.; Yoshizawa, K.; Shimizu, K. *Chem. Eur. J.* **2017**, *23*, 1001-1006.

(13) Takeda, Y.; Tamura, M.; Nakagawa, Y.; Okumura, K.; Tomishige, K. *ACS Catal.* **2015**, *5*, 7034-7047.

(14) Kandel, K.; Chaudhary, U.; Nelson, N. C.; Slowing, I. I. *ACS Catal.* **2015**, *5*, 6719-6723.

(15) Manyar, H. G.; Paun, C.; Pilus, R.; Rooney, D. W.; Thompson, J. M.; Hardacre, C. *Chem. Commun.* **2010**, *46*, 6279-6281.

(16) Brewster, T. P.; Miller, A. J.; Heinekey, D. M.; Goldberg, K. I. *J. Am. Chem. Soc.* **2013**, *135*, 16022-16025.

(17) Naruto, M.; Saito, S. *Nat. Commun.* **2015**, *6*, 8140.

(18) Cui, X.; Li, Y.; Topf, C.; Junge, K.; Beller, M. *Angew. Chem. Int. Ed.* **2015**, *127*, 10742-10745.

(19) Korstanje, T. J.; van der Vlugt, J. I.; Elsevier, C. J.; de Bruin, B. *Science* **2015**, *350*, 298-302.